Supplementary Information for Modulating Roughness and Ripple Dynamics in Hexagonal Boron Nitride via Defect Engineering

Md. Rakib Hassan, Owen R. Dunton, and Francis W. Starr

Contents

1 Parameterization, validation and Speed of ACE-hBN20

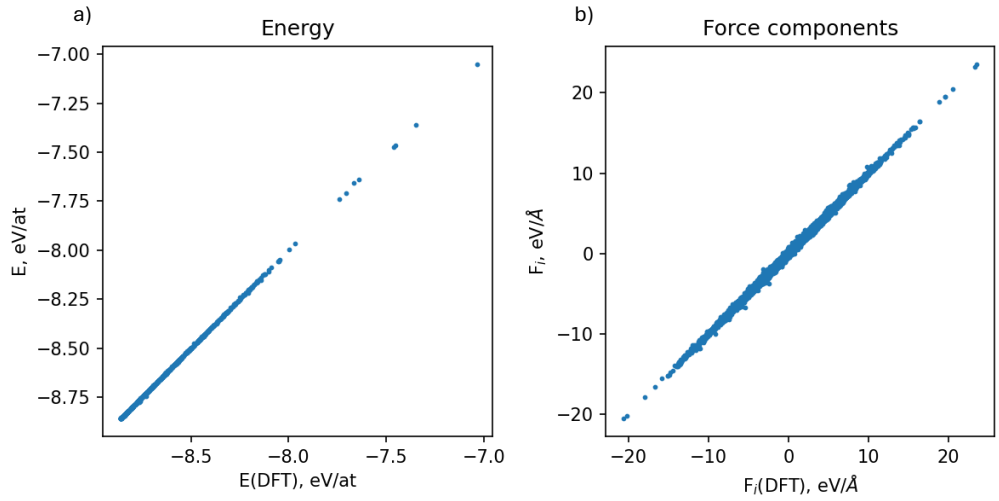

Fig. S1: Parity plots comparing the ACE-hBN20 model's prediction for (a) energies and (b) forces with DFT for the random 20% test set.

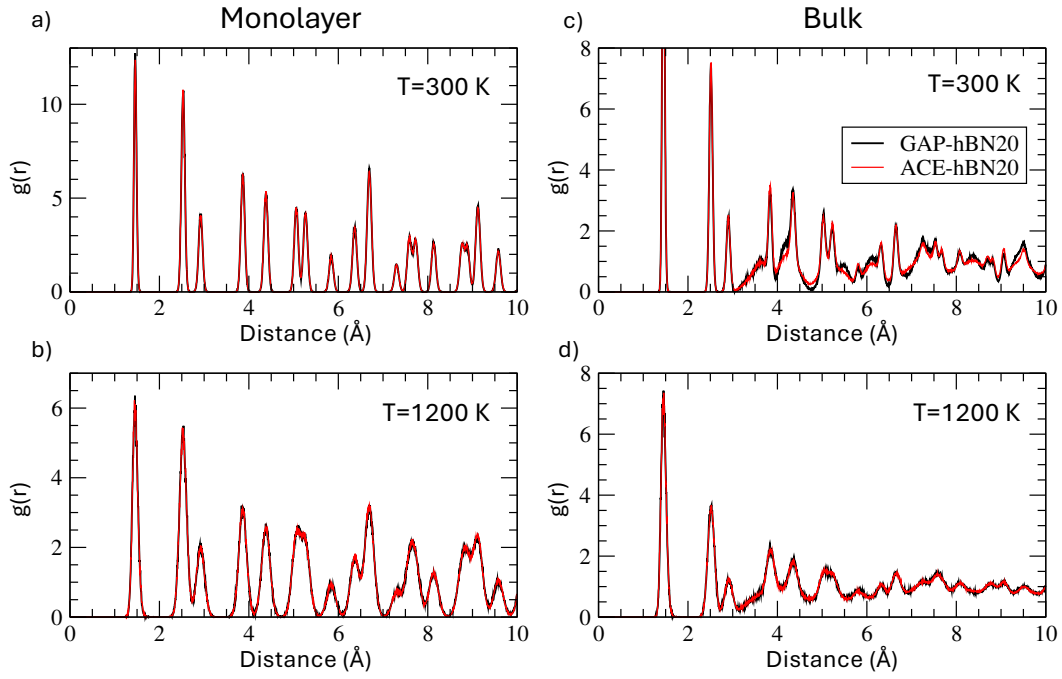

Fig. S2: Radial distribution function g(r) predicted by ACE-hBN20 compared with those predicted by GAP-hBN20 for (a) 300 K monolayer, (b) 1200 K monolayer, (c) 300 K bulk, (d) 1200 K bulk.

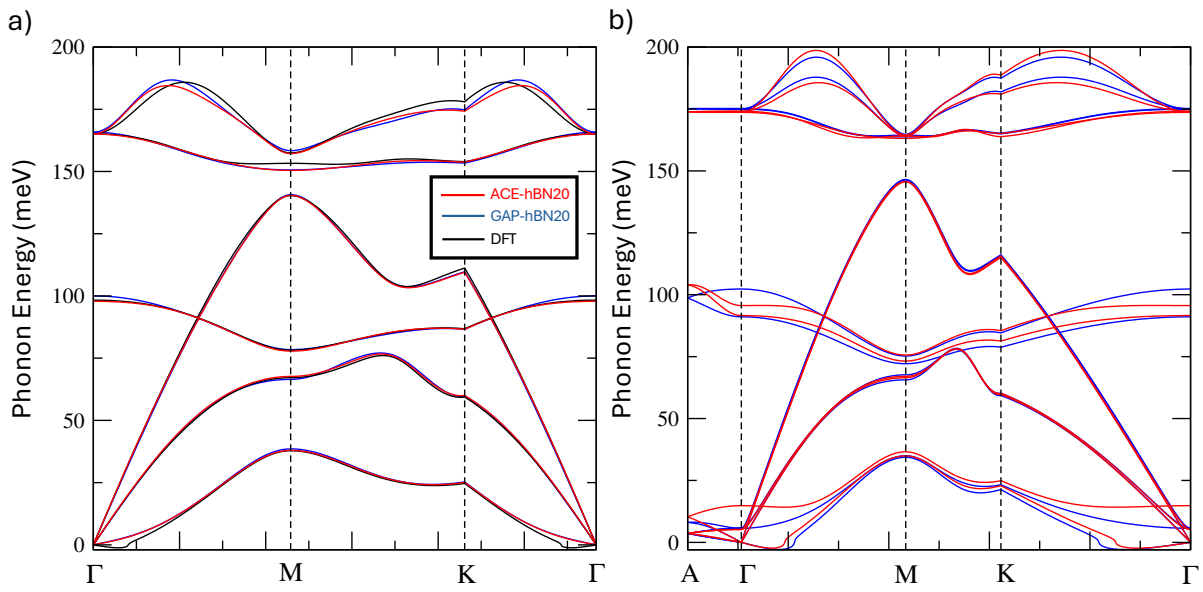

Fig. S3: Phonon dispersion curves for (a) monolayer hBN and (b) bulk hBN. ACE refers to ACE-hBN20.

For ACE-hBN20, we use a simple linear ACE model, where the energy of an atom environment is directly equal to a single atomic property, or expansion in terms of its neighbors' coordinates. Exponentially-scaled Chebyshev polynomials are selected to form the radial component of the many-body basis functions.

Figure S1 shows the parity plot for the randomly selected 20% test set, demonstrating agreement between the forces and energies predicted by ACE-hBN20 and DFT for configurations not included in the training set. We also show the radial distribution function $g(r)$ of ACE-hBN20 in comparison with GAP-hBN20, again for monolayer and bulk hBN configurations equilibrated at 300 and 1200 K. Figure S2 shows identical structures predicted by these two potentials in all four cases, with even near-perfect agreement in the bulk case at 300 K. Figure S3 shows the phonon dispersion curve predicted by ACE-hBN20 for monolayer and bulk hBN. Similar to the results from ACE-BN25, ACE-hBN20 agrees very strongly with DFT and GAP-hBN20, which was validated against experiment. Finally, Fig. S4 shows the computational efficiency of the GAP-hBN20, MTP, and ACE models with and without GPU. This is plotted as the number of nanoseconds able to be

simulated in a day at various system sizes on a single CPU (or 1 CPU & 1 GPU for the ACE with GPU case). The performance of ACE-BN25 and ACE-hBN20 are essentially identical.

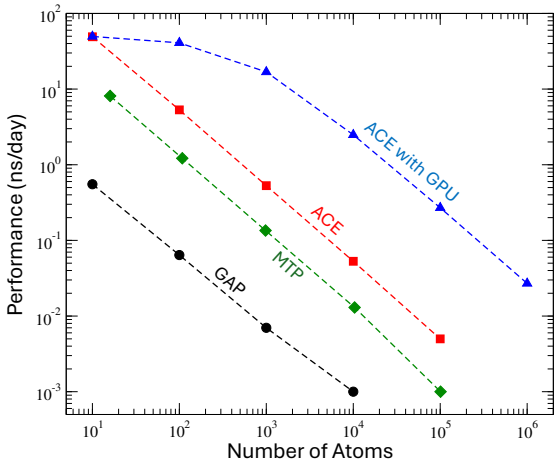

Fig. S4: Computational efficiency of the ACE model with and without GPU acceleration, compared with the GAP-hBN20 and MTP. Note that GPU parallelization is fully realized at systems larger than 1000 atoms.

2 ACE-BN25 Parametrization and Training Set Generation

For ACE-BN25, we use a Finnis-Sinclair [1] style nonlinear embedding – as opposed to a simple linear model – where the energy depends linearly on one atomic property and on the square root of a second. Additionally, we switch our radial basis to simplified spherical Bessel functions following the Si potential of Ref. [2].

In both the cases of 2D monolayer and 3D bulk, we prepare amorphous configurations by performing equilibrium liquid simulations using the Lennard-Jones potential, with the zero-crossing distance selected as the sum of atomic radii for each pairwise interaction (N-N, B-B, or B-N). We then perform DFT calculations of these resulting configurations in Quantum Espresso [3, 4] to generate accurate forces and energies. To generate a substantial set of cubic BN configurations, we subject a perfect sc lattice to random perturbations before a DFT calculation. Specifically, the position of each atom is perturbed from its equilibrium lattice site by a random distance smaller

than an eighth of the lattice constant, and then the entire cell is subjected to random shear and scale transformations.

Pure boron configurations are added to the training set by incorporating the training set of the boron potential of Ref. [5], containing multiple crystal structures. The forces and energies of these configurations are recomputed in Quantum Espresso to ensure compatibility with our PBE-based training set. We generate additional pure boron configurations with 2D geometries to ensure B-B bonds in monolayer structures are incorporated in the training set. This is done by generating a perfect boron monolayer, and subjecting it to 20 perturbations for 20 unique configurations. Finally, we take pure nitrogen structures from the Materials Project [6] database, including three cubic crystals, two hexagonal crystals, two tetragonal crystals, an orthorhombic crystal, and a trigonal crystal. Each of these structures is subject to 10 unique perturbations, each of which is incorporated in the training set.

All DFT simulations are done using the PBE functional; we use the pseudopotentials `B.pbe-n-kjpaw_psl.1.0.0.UPF` and `N.pbe-n-kjpaw_psl.1.0.0.UPF` for boron and nitrogen, respectively. Our kinetic energy cutoff is set to 80 Ry for the wavefunctions, and 320 Ry$= 4 \cdot 80$ Ry for the charge density. The convergence threshold for ionic minimization is set to 10^{-6} eV for the energy and 10^{-3} eV/Åfor the forces. Electrons occupy eigenstates according to a gaussian smearing to account for partial occupation near the Fermi level, with the smearing width set to 0.05 eV. We include a Grimme-D3 style semiemperical dispersion correction with Becke-Johnson damping on top of the DFT [7, 8, 9]. This is done following Ref. [5], which does so to match the experimentally known interlayer spacing of bulk hBN.

3 ACE-BN25 Validation

3.1 Parity Plots

Figure S5 shows parity plots for the randomly selected test set, where the ACE-BN25 model's predictions for (a) energies and (b) forces are plotted against the DFT labels. These show nearly perfect agreement between ACE and DFT on the test set, indicating the potential's robustness for predicting interatomic interactions for environments not included in the training set.

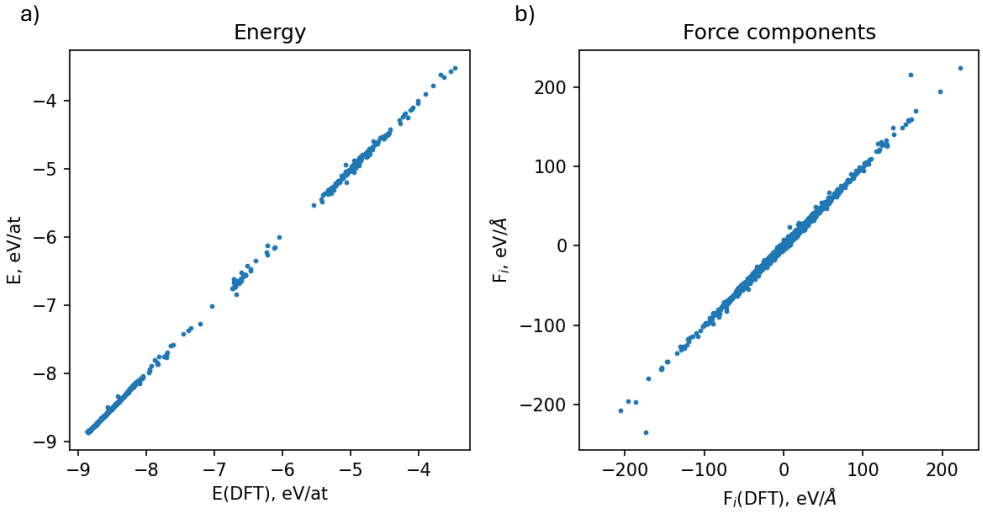

Fig. S5: Parity plots comparing the ACE-BN25 models' prediction of (a) energies and (b) forces with DFT for the test set.

3.2 Interlayer Separation

We perform equilibrium simulations of bulk hBN in the isothermal-isobaric ensemble at room temperature and atmospheric pressure in order to determine the density and interlayer separation predicted by both ACE models. We find that both ACE-hBN20 and ACE-BN25 predict an equilibrium separation of 3.36 Å, within 1% of the experimentally known separation distance of 3.33 Å [10]. We also find the density under these conditions for both potentials $\rho(T = 300\text{ K}, P = 1\text{ ATM})$= 2.24 gm/cm^3, which lies within the range of experimentally reported densities [11, 12, 13].

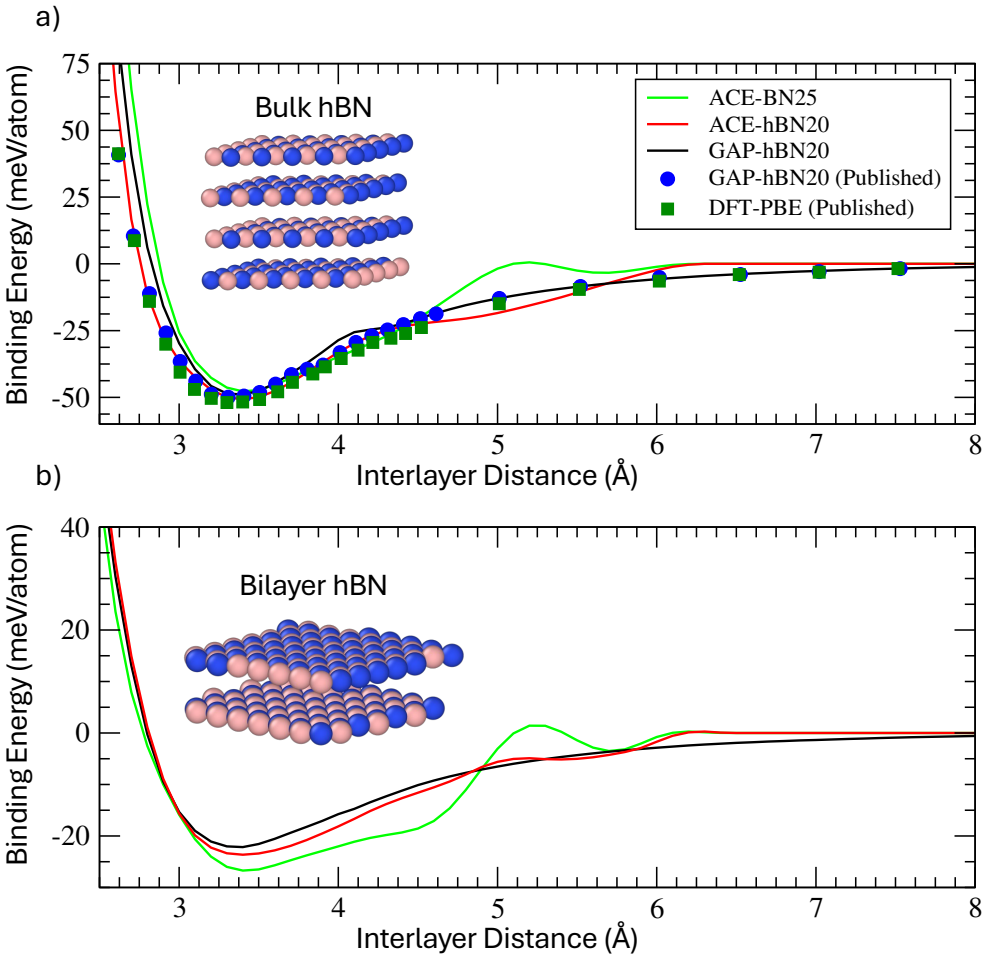

Fig. S 6: Binding energy of (a) bulk hBN and (b) bilayer hBN as a function of the interlayer separation distance for GAP-hBN20, ACE-BN25, and ACE-hBN20. Published results for GAP-hBN20 and DFT from Ref. [5] are included for the bulk case.

We also include for validation of both ACE-hBN20 and ACE-BN25 the interlayer binding energy as a function of the distance between layers for bilayer hBN, as well as a bulk of stacked sheets. Data for GAP-hBN20, ACE-hBN20, and ACE-BN25 are shown for both structures in Fig. S6, and published GAP-hBN20 and DFT data are also included for bulk hBN. The qualitative behaviors of both ACE-hBN20 and ACE-BN25 agree with GAP-hBN20 and DFT, though there are slight quantitative differences in the results from ACE-BN25 at larger separation for both the bulk and bilayer case. Critically, both ACE models have a minimum near the experimental equilibrium separation and a repulsive wall at shorter separation. We thus do not consider the oscillations in

the binding energy at large separation to be a major shortcoming of the ACE-BN25 model, since most simulations of bulk and bilayer hBN will be done at the experimental separation, which the model accurately captures.

3.3 Validation of ACE-BN25 for pure Boron

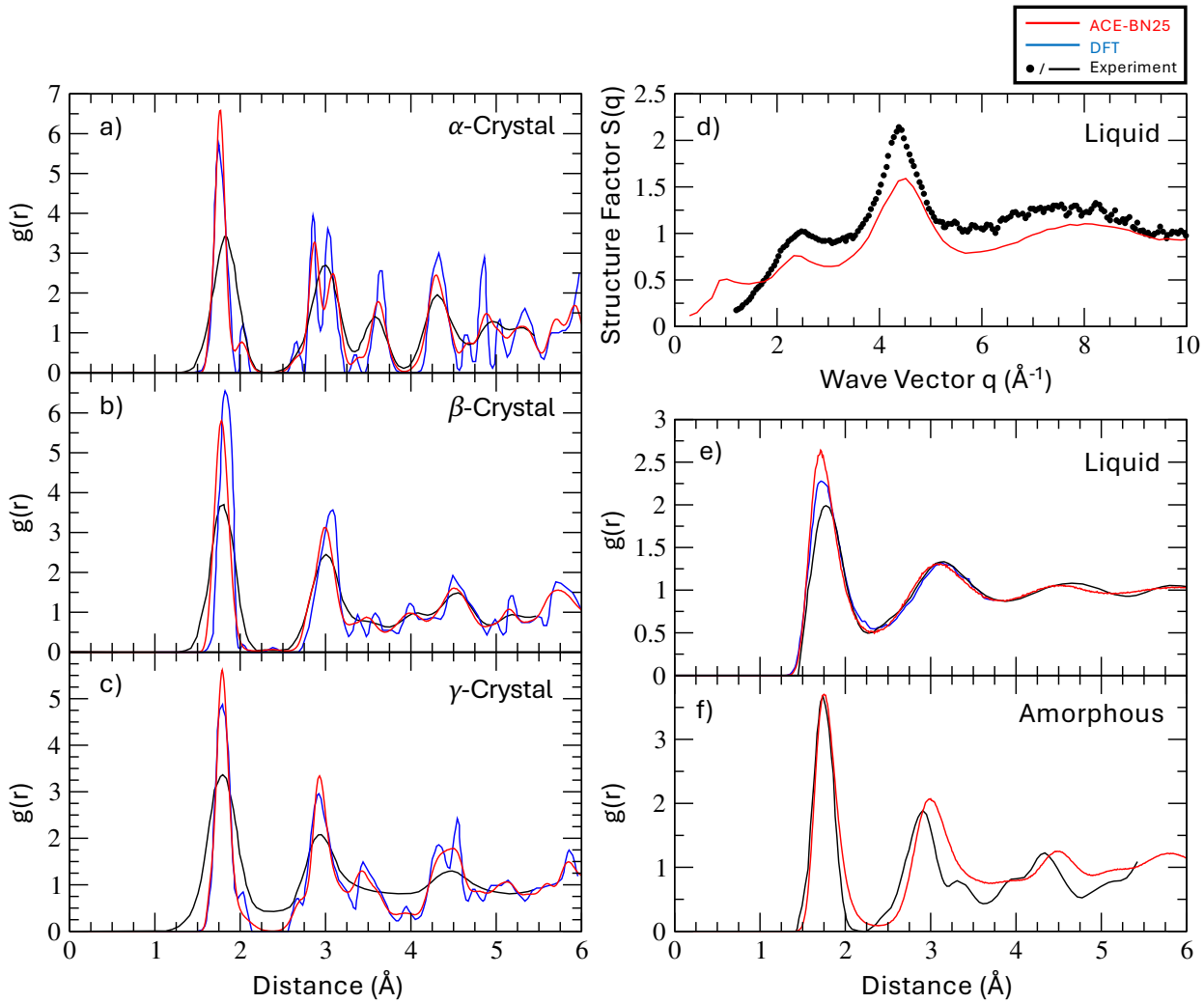

Fig. S 7: The structures of pure boron predicted by ACE-BN25 in comparison with DFT and experimental results. The radial distribution function $g(r)$ for α, β, and γ boron crystals are shown in (a)-(c), respectively. The liquid structure is demonstrated via (d) the structure factor $S(q)$ and (e) $g(r)$, and the amorphous structure (f) is shown via $g(r)$. Experimental and DFT data are taken from Ref. [5, 14].

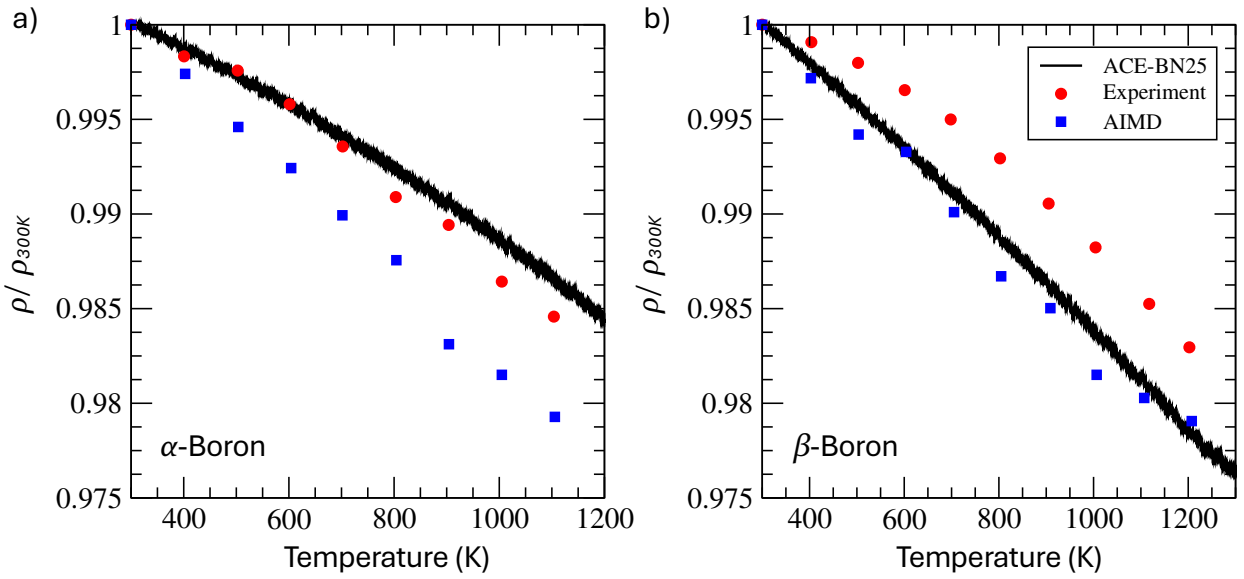

Fig. S8: The thermal expansion of the α- and β-Boron crystals, plotted as the ratio of the density at a given temperature to that at $T = 300$ K. DFT and experimental data taken from Ref. [5, 15, 16].

Since the revised training set of ACE-BN25 contained a set of boron configurations sufficient to train a stand-alone boron potential, we include a validation of its performance for pure boron. Figure S7(a)-(c) shows $g(r)$ of boron crystals of types α, β, and γ, equilibrated using ACE-BN25, in comparison with experimental and DFT results. Starting configurations are sourced from Materials Project [6]. The peak locations of the system prepared with ACE-BN25 agree with those of both DFT and experimental results, indicating that ACE-BN25 accurately predicts the structure of all three crystal types. We also validate the structure for disordered states; Fig. S7(d) shows the structure factor for liquid boron, and Fig. S7(e) & (f) show g(r) for liquid and amorphous boron, respectively. Qualitative agreement with experiment is clear in all cases, and the liquid radial distribution function agrees quantitatively with both experiment and DFT.

The thermal expansion on heating is shown in Fig. 8 for both the α and β crystal types. These are included as the ratio between the density $\rho(T)$ and its value at $T = 300$ K, and are plotted with results from *ab-initio* molecular dynamics (AIMD) and experiment to show the agreement with known results.

We do not perform a similar validation on pure nitrogen, since the training set contains only crystalline phases and does not adequately sample liquid and gaseous regions of its phase diagram. As a consequence, the potential incorrectly predicts solid nitrogen above the experimental melting temperature. We do not consider this a significant shortcoming, since liquid and gaseous nitrogen are already effectively modeled through simple analytic methods. Our goal is the development of a potential for monolayer hBN that can support defects, as opposed to a potential transferable across all stoichiometries of boron and nitrogen.

4 Spontaneous $4|8$ Defect Formation at High Temperature

Defect type \ Potential	DFT	GAP-hBN20	ACE-hBN20	ACE-BN25	EXTEP	MTP
Pristine	0	0	0	0	0	0
SW	7.26	15.96	17.169	8.474	8.838	21.415
B-centered 4|8	10.306	10.34	10.72	10.613	27.188	11.001
N-centered 4|8	8.074	8.496	10.324	8.492	40.064	9.307
Divacancy	28.034	25.449	27.173	25.999	26.102	26.3
B-monovacancy	17.443	16.7	24.791	13.148	18.644	13.962
N-monovacancy	17.228	13.139	10.286	17.545	13.742	18.457
B-interstitial	8.788	22.093	9.068	10.54	5.66	34.913
N-interstitial	5.905	25.3	60.721	4.631	11.4	73.212

Table S1: Formation energies (eV) of defect types calculated using different interatomic potentials.

In pristine hBN, the primary defects that can form spontaneously at high temperatures are Stone-Wales (SW) rotations and square-octagon (4|8) pairs. While SW defects (5|7 pairs) are common in graphene, 4|8 defects are unique to hBN due to its alternating atomic composition, which favors heteroelemental bonds. Liu et al. [17] first identified the 4|8 dislocation structure in hBN via first-principles calculations, demonstrating that it has lower energy than the corresponding 5|7 (SW) pairs, as the latter involve unfavorable homonuclear bonds (B-B or N-N). Their work focused on grain boundaries, where 4|8 pairs can exist in isolation or chains to accommodate

misorientation.

Forming an isolated 4|8 defect in pristine hBN without introducing a grain boundary is topologically challenging, as it would disrupt the lattice continuity. Simulations using the ACE-BN25 potential at high temperatures reveal that 4|8 defects do form in pristine hBN, but they appear in triplets to avoid the formation of dislocations.These triplets come in two variants: boron-centered (B-centered 4|8) and nitrogen-centered (N-centered 4|8). Each triplet can form through two mechanisms. Figure 3 in the main paper illustrates the mechanisms for an N-centered 4|8 triplet: either i) the surrounding three boron atoms move cyclically around the central nitrogen, or ii) one boron moves oppositely to the parallel motion of the other two; the same mechanism applies to B-centered 4|8 triplets.

Liu et al. [17] reported that a single 4|8 defect is energetically favorable over a single SW defect by approximately 1 eV. This holds in our calculations as well (Table S1). However, SW defects naturally occur in pairs (two 5|7 defects), while 4|8 defects form in triplets (three 4|8 defects). Consequently, the total energy of an SW pair is lower than that of a 4|8 triplet, making SW defects more energetically stable. As a result, near the melting temperature, where defects form spontaneously in pristine hBN, SW defects are more frequent than 4|8 defects.

A critical issue with other machine-learned potentials (GAP-hBN20, ACE-hBN20, MTP) is that they predict SW pairs to have higher energy than 4|8 triplets which contradicts DFT benchmarks. In the EXTEP classical potential, 4|8 triplets exhibit unrealistically high energies ($\sim$27 eV for B-centered and $\sim$40 eV for N-centered), rendering spontaneous formation nearly impossible. Considering all scenarios, the ACE-BN25 potential excels in capturing accurate defect energies (compared to DFT) and the high-temperature dynamics of hBN, enabling reliable predictions of spontaneous defect formation.

5 Angle Correlation Function

To quantify the rippling dynamics in hBN we follow a procedure described by Thiemann et al. [18]. We define the local inclination θ_i for each atom i as the angle between the atomic normal vector $\vec{n}_i$ and the out-of-plane z-direction. The atomic normal vector $\vec{n}_i$ is perpendicular to the local surface A_i approximated around atom i. We identify neighboring atoms within 4.5 Å of atom i and fit a second-order polynomial $z(x,y) = a + bx + cy + dxy + ex^2 + fy^2$ to their relative heights. The normal vector is then $\vec{n}_i = [-b, -c, 1]^T$, and the inclination is $\theta_i = \arccos\left(1/\sqrt{b^2+c^2+1}\right)$. The root-mean-square inclination $\theta_{\text{rms}} = \sqrt{\langle\theta^2\rangle}$ measures corrugation, where the average is over all atoms and frames. The normalized autocorrelation function $C_\theta(\tau) = \langle\theta(\tau)\theta(0)\rangle/\langle\theta^2\rangle$ probes dynamics, decaying to a plateau $C_\theta(\tau\to\infty) \approx 0.8$ for dynamic ripples in pristine hBN, and approaching 1 for static configurations.

Figure 9 illustrates $C_\theta(\tau)$ for pristine hBN and defective systems. For pristine hBN (panel a), multiple runs converge to a consistent plateau, confirming dynamic behavior. In defective cases (panels b-f), higher concentrations elevate the plateau, with SW defects showing the most pronounced shift. This defect-specific response highlights how certain defects pin ripples, while others (e.g., vacancies) do not alter dynamics, consistent with hBN's polar bonding.

We also present the atomically resolved long-time angle autocorrelation function, $C_\theta(\tau\to\infty)$, alongside the virial contribution to the normal stress, $\langle|W_{zz}|\rangle$, in Figure 10. Panels (a) and (b) show these quantities for SW defects, while panels (c) and (d) provide the corresponding maps for B-centered 4|8 defects at the same defect concentration for comparison. In both cases, regions around defects exhibit bright patterns that spatially coincide, indicating areas of pinned atoms. This correspondence directly confirms that the observed crossover from dynamic to static ripples arises from interactions between SW defects. As demonstrated in Figure 5 of the main paper, SW defects exhibit the strongest interactions among all defect types considered, making them the primary drivers of this crossover phenomenon. The atomically resolved maps show that high stress regions

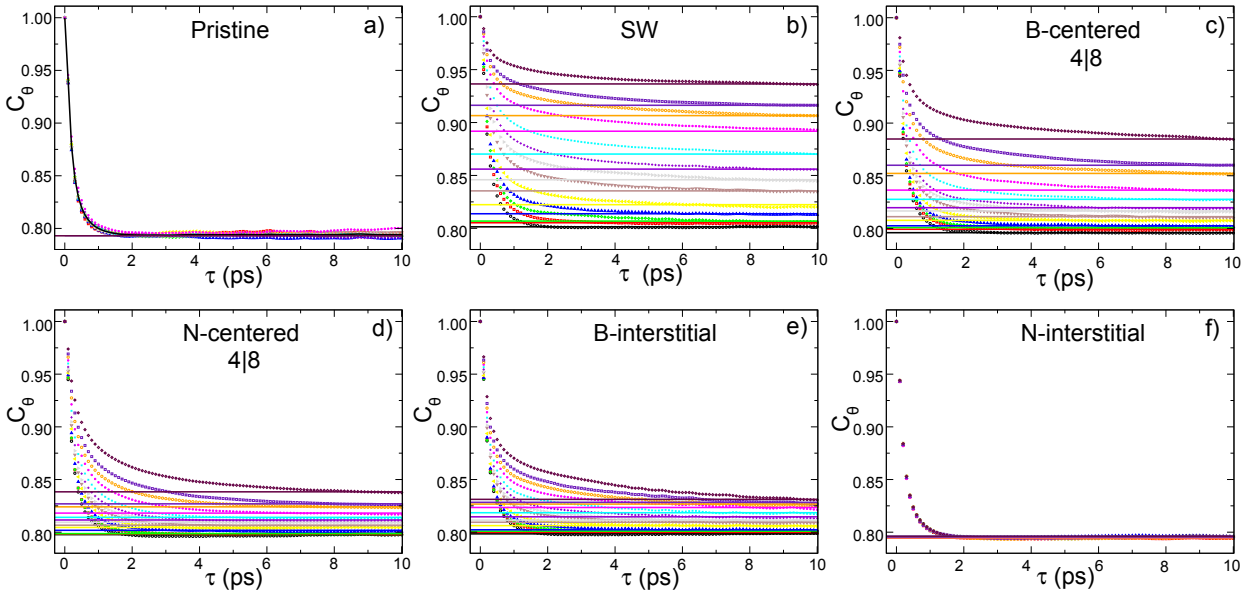

Fig. S9: Angle autocorrelation function $C_\theta(\tau)$ versus time for pristine hBN and various defect types at different concentrations. (a) Ten independent runs of pristine hBN converging to a plateau value of ~ 0.793 (black line shows the average of all 10 runs). hBN with (b) SW defects, (c) B-centered 4|8 defects, (d) N-centered 4|8 defects, (e) B-interstitial defects, and (f) N-interstitial defects. Different colors represent varying defect concentrations, with corresponding solid lines indicating the plateau value. A time scale of $\tau = 10$ ps is sufficiently long to approximate $f(\tau \rightarrow \infty)$. As defect concentration increases from low (black) to high (maroon), the plateau value rises for SW, 4|8 (B- and N-centered), and B-interstitial defects, signaling a crossover to static rippling (see Fig. 5(a) in the main paper). Vacancy defects (not shown) exhibit no change from the pristine value, similar to N-interstitials; N-interstitials are representative of defects with minimal impact.

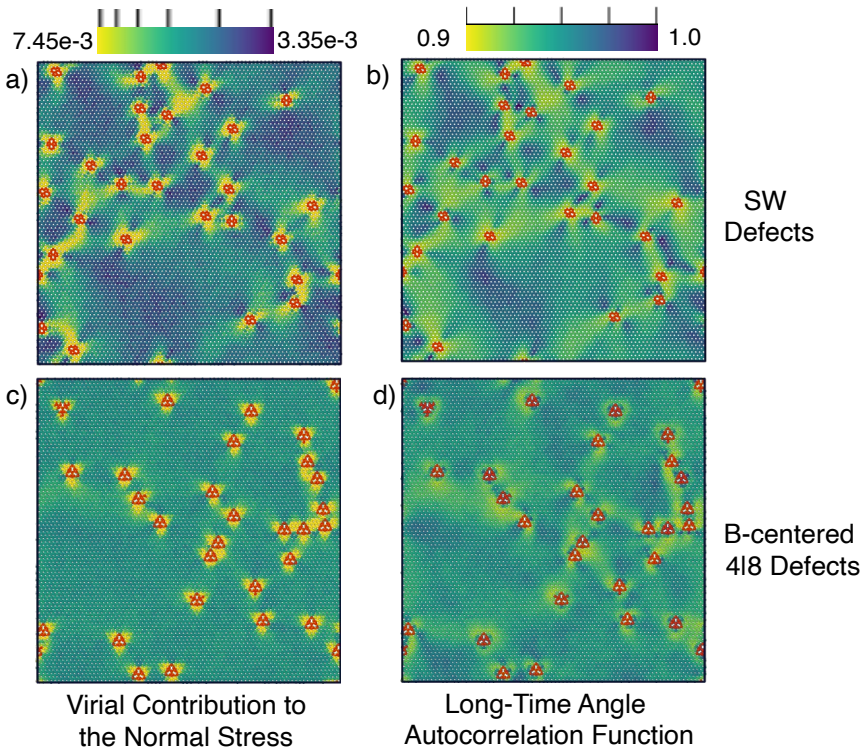

Fig. S10: Microscopic origin of the defect-induced dynamical crossover in hBN with SW defects. (a) Atomically resolved virial contribution to the normal stress $\langle |W_{zz}| \rangle$ (log scale), with high stress concentrated at defect sites. (b) Atom-resolved long-time angle autocorrelation $C_\theta(\tau \to \infty)$ (linear scale); low-correlation regions indicate dynamic mobility, while high-correlation regions reveal static pinning. In both cases, defects are marked with red. The spatial overlap highlights that elastic interactions between defects, emerging at high concentrations, drive the crossover to static rippling.

correspond to areas of high inclination correlation, whereas dynamically mobile regions remain low in both stress and correlation. This spatial overlap provides direct microscopic evidence that static ripple formation is mediated by defect-induced constraints, emerging prominently at higher SW defect concentrations. The comparison with B-centered 4|8 defects clearly shows weaker interactions in both heat maps, with fainter and less extensive bright patterns around the defect sites.

References

[1] Finnis, M. W. & Sinclair, J. E. A simple empirical N-body potential for transition metals. *Philosophical Magazine A* **50**, 45–55 (1984).

[2] Lysogorskiy, Y. *et al.* Performant implementation of the atomic cluster expansion (PACE) and application to copper and silicon. *npj Computational Materials* **7**, 97 (2021).

[3] Giannozzi, P. *et al.* QUANTUM ESPRESSO: a modular and open-source software project for quantum simulations of materials. *Journal of Physics: Condensed Matter* **21**, 395502 (2009).

[4] Giannozzi, P. *et al.* Advanced capabilities for materials modelling with Quantum ESPRESSO. *Journal of Physics: Condensed Matter* **29**, 465901 (2017).

[5] Thiemann, F. L., Rowe, P., Müller, E. A. & Michaelides, A. Machine learning potential for hexagonal boron nitride applied to thermally and mechanically induced rippling. *The Journal of Physical Chemistry C* **124**, 22278–22290 (2020).

[6] Jain, A. *et al.* Commentary: The Materials Project: A materials genome approach to accelerating materials innovation. *APL Materials* **1**, 011002 (2013).

[7] Grimme, S., Antony, J., Ehrlich, S. & Krieg, H. A consistent and accurate ab initio parametrization of density functional dispersion correction (dft-d) for the 94 elements h-pu. *The Journal of Chemical Physics* **132**, 154104 (2010).

[8] Grimme, S., Ehrlich, S. & Goerigk, L. Effect of the damping function in dispersion corrected density functional theory. *J Comput Chem.* **32**, 1456–65 (2011).

[9] Becke, A. D. & Johnson, E. R. A density functional model of the dispersion interaction. *The Journal of Chemical Physics* **123**, 154101 (2005).

[10] Henck, H. *et al.* Direct observation of the band structure in bulk hexagonal boron nitride. *Physical Review B* **95**, 085410 (2017).

[11] Yang, H. *et al.* Low temperature self-densification of high strength bulk hexagonal boron nitride. *Nature Communications* **10**, 854 (2019).

[12] Song, W., Liu, D., Wang, F. & Zhang, L. The development of hexagonal boron nitride crystal growth technologies and their applications in neutron detection. *Nanomaterials* **15**, 1256 (2025).

[13] Yang, Y., Peng, Y., Farooq Saleem, M., Chen, Z. & Sun, W. Hexagonal boron nitride on III–V compounds: A review of the synthesis and applications. *Materials (Basel, Switzerland)* **15**, 4396 (2022).

[14] Krishnan, S., Ansell, S., Felten, J. J., Volin, K. J. & Price, D. L. Structure of liquid boron. *Physical Review Letters* **81**, 586–589 (1998).

[15] Cherednichenko, K. A. & Solozhenko, V. L. Thermal expansion of α-boron and some boron-rich pnictides. *Solid State Communications* **303-304**, 113735 (2019).

[16] Lundström, T., Lönnberg, B. & Bauer, J. Thermal expansion of β-rhombohedral boron. *Journal of Alloys and Compounds* **267**, 54–58 (1998).

[17] Liu, Y., Zou, X. & Yakobson, B. I. Dislocations and grain boundaries in two-dimensional boron nitride. *ACS Nano* **6**, 7053–7058 (2012).

[18] Thiemann, F. L., Scalliet, C., Müller, E. A. & Michaelides, A. Defects induce phase transition from dynamic to static rippling in graphene. *Proceedings of the National Academy of Sciences* **122**, e2416932122 (2025).